THE ASTROPHYSICAL JOURNAL, 470:469–478, 1996 October 10


# GAMMA-RAY PULSARS: RADIATION PROCESSES IN THE OUTER MAGNETOSPHERE

ROGER W. ROMANI[1]
Department of Physics, Stanford University, Stanford, CA 94305-4060; rwr@astro.stanford.edu
*Received 1996 January 5; accepted 1996 May 2*

## ABSTRACT

We describe an emission model for $\gamma$-ray pulsars based on curvature radiation-reaction–limited charges in the outer magnetosphere. We show how pair production on thermal surface flux can limit the acceleration zones; estimates for the efficiency of GeV photon production $\eta_\gamma$ and the $\gamma$-ray beaming fraction are derived, including their dependence on pulsar parameters. In general, $\eta_\gamma$ increases with pulsar age but is decreased for low magnetic fields and for small magnetic inclinations. We argue that this produces GeV pulse profiles, curvature spectra, and detection statistics consistent with the observations. We also describe the optical through X-ray pulsar synchrotron spectrum and the spectral variations with pulsar phase. A test computation for Vela-like parameters reproduces phase-resolved GeV spectra consistent with those observed by EGRET. Finally, we comment on very high energy pulsed emission and particle production and note extensions needed to allow a more complete pulsar model.

*Subject headings:* gamma rays: theory — pulsars: general — radiation mechanisms: nonthermal

## 1. INTRODUCTION

Isolated spin-powered pulsars are very prominent in the high-energy sky. In the GeV $\gamma$-ray range, in particular, the EGRET experiment on the *Compton Gamma Ray Observatory* (*CGRO*) has now detected pulsed signals from at least six objects. In addition $\sim 30$ point sources are found at low latitudes ($b < 10°$) along the Galactic plane (Thompson et al. 1996). The identification of one of these objects (Geminga = PSR 0630+18) with a pulsar not visible in the radio (Halpern & Holt 1992) has made the connection with young isolated pulsars particularly appealing.

In the outer magnetosphere picture of Romani & Yadigaroglu (1995, hereafter RY), we developed a model for the beaming of high-energy $\gamma$-ray emission that reproduces the observed properties of individual $\gamma$-ray pulsars, including high-energy pulse profiles, the relation to the radio pulses, and the nondetection of pulsars such as PSR B0656+14. In Yadigaroglu & Romani (1995, hereafter YR), it was shown that the statistics of $\gamma$-ray pulsars and Geminga-like objects were in good agreement with the predictions of our $\gamma$-ray pulsar model for pulsar properties entirely consistent with those inferred from radio surveys. These results extended earlier population studies based on extrapolation from the observed pulsars (cf. Halpern & Ruderman 1993; Helfand 1994). However, the luminosity law used in the population estimates of YR was based on a standard phenomenological fit of efficiency versus spin-down age; a more physically based description of the gamma-ray efficiency is needed to follow dependence on magnetic field and other pulsar parameters.

A second class of important pulsar models are those placing the emission zone at the polar cap, with emission altitudes of $\sim 10^4$ cm to several neutron star radii (Harding & Daugherty 1993; Dermer & Sturner 1994). While these polar cap models have difficulty in reconciling the observed $\gamma$-ray pulses with the known radio pulsar geometry, and while substantial modification of the standard polar cap picture is needed to derive reasonable pulse profiles and pulsar numbers, these computations have had good success in obtaining high-energy spectra similar to those observed for the Vela pulsar and other young objects. Moreover, both the resonant Compton scattering–based model of Sturner, Dermer, & Michel (1995) and, especially, the curvature radiation–based model of Daugherty & Harding (1996) have shown that polar cap radiation schemes can produce spectral index variations through the observed pulse similar to those measured for Vela by EGRET (Kanbach et al. 1994). Similar results have been difficult to obtain for radiation from the outer magnetosphere. Chiang & Romani (1994) were able to show that because of the variation of the magnetic field through the radiation zone, spectral index changes were expected during the pulse in a radiation model based on the outer gap picture of Cheng, Ho, & Ruderman (1986, hereafter CHR). However, they also found that this scheme failed to produce self-consistently the soft photon fields needed to support the gap closure, even for the Crab pulsar, so that further study of radiation processes in the outer magnetosphere was required.

In this paper we describe a revised picture of gap closure and radiation physics in the outer magnetosphere, after reviewing briefly difficulties with the CHR scheme (§ 2). Although this radiation model shares the limitation of present cap models in that it does not start from a first principles computation of acceleration fields and particle densities, we find that a simple premise for the acceleration voltage allows a computation of the pulsar efficiency and its variation with spin parameters (§ 3); the predicted luminosities compare well with those observed by EGRET, and very high apparent efficiencies can be naturally accommodated in this model. In § 4 we turn to the spectrum predicted by our radiation model. After describing the phase-averaged pulsar spectrum and dependence of spectral breaks on pulse parameters, we show how the high-energy spectrum should vary through the pulse and present a test computation for Vela (§ 5). The computed phase-resolved spectra are compared with EGRET results. We conclude in § 6 by noting three-dimensional extensions to the spectral computations that should provide more precise models and by describing extensions of the pulse modeling to both lower and higher photon energies.

[1] Alfred P. Sloan Fellow.

## 2. OUTER MAGNETOSPHERE RADIATION AND GAP CLOSURE

CHR developed a version of an outer magnetosphere $\gamma$-ray emission zone in which acceleration in "Holloway (1973) gaps" above the null charge surface brought a corotation charge density of particles to Lorentz factors $\gamma \sim 10^{7.5}$. These primary charges ($e_1$) were radiation-reaction limited by inverse Compton scattering on a posited dense bath of soft photons. The primary energy was thus radiated in a $\sim$1–10 TeV Compton spectrum ($\gamma_1$) that was fully absorbed via pair production on the same soft photon bath ($\gamma_3$). The resulting secondary charges ($e_2$) suffered strong synchrotron losses that resulted in a power-law spectrum ($\gamma_2$) of secondary radiation identified with the high-energy pulses observed from the Crab and the Vela pulsars. In the CHR model the gap was assumed symmetric, so that primary charges were produced all along the gap zone; one sign would accelerate and produce an outward beam of radiation, while the opposite sign would similarly produce an inward beam of $\gamma$-ray flux. In the final step of this picture, the opposing $\gamma_2$ beams provided for further pair production; the resulting low-energy $e_3$ pairs were argued to produce the soft tertiary photon bath ($\gamma_3$) needed for the original gap closure.

Since this model was presented, several difficulties in explaining the observed pulsar radiations have arisen. For example, Chiang & Romani (1992) showed that the CHR picture in which a single bundle of field lines was active in the outer magnetosphere and which provided a double pulse by utilizing the opposing beams from opposite gaps did not produce pulse profiles like those observed. Moreover, in the original CHR model, it proved difficult to have a gap active for pulsar periods much larger than $\sim$0.1 s, so that objects such as Geminga were difficult to understand (although Chen & Ruderman 1993 argued that highly inclined dipole rotators $\alpha \sim \pi/2$ might remain active in the Geminga regime). A key difficulty with this picture is that it was essential for the gap to be optically thick for pair production to absorb the (unobserved) TeV photons produced by the primary particles. This in turn required very high luminosities for ($\gamma_3$) which were in the near-IR (Vela) to optical-UV bands (Geminga); the required fluxes were generally orders of magnitude larger those observed from these objects (cf. Usov 1994). In fact, in a computation of the CHR scheme, following the variation in the pair production and radiation efficiencies as particles moved through the outer magnetosphere gap, Chiang & Romani (1994) were unable to obtain sufficient tertiary flux for self-consistency, even for the Crab pulsar. Finally, the symmetry of the gaps suggests that the neutron star surface heating from the downward-directed particles and radiation might be excessive, as noted by Arons & Scharleman (1979). Usov (1994) showed that this argument applied to CHR-type outer magnetosphere acceleration produced significant excess thermal flux for objects such as Geminga.

CR noted that if the outer gap spanned the entire set of field lines crossing the null charge $\boldsymbol{\Omega} \cdot \boldsymbol{B} = 0$ surface above the surface of last closed field lines, then the outward-directed beam from a single pole could produce pulse profiles quite similar to those observed from high-energy pulsars. In RY this geometrical model of pulsar beaming was further developed starting from the vacuum dipole solution and showing that observed pulse profiles, phase lags from the radio emission, and polarization properties could be naturally reproduced. Noting that the gap width controlled both the high-energy beam extent and the $\gamma$-ray efficiency, YR showed how a synthesis of the Galactic neutron star population produced $\gamma$-ray pulsars in good accord with those observed and implied that the bulk of the unidentified sources are indeed isolated $\tau \sim 10^{4.5}$ yr pulsars. For details of the beaming geometry see RY; the population work is extended to include more precise description of local high-mass star formation, candidate identifications for the EGRET plane sources, and comparison with model luminosity functions in Yadigaroglu & Romani (1996).

To support these successes, it is important to lay out the basic physics of gap closure for this outer magnetosphere model. Our model is based on curvature radiation in the outer magnetosphere and so has important antecedents in the work of Morini (1983) and Ochelkov & Usov (1980). There is also similarity to the $\gamma$-ray production in the slot gap of Arons (1981), although the basic geometrical and electrodynamic assumptions follow those of CHR more closely. Since the outer gap emission zones typically start from $\gtrsim$10 neutron star radii, high-order magnetic multipoles and offset surface dipoles will have little effect on the magnetic field structure (although they might be quite important for the charge-density boundary conditions at the lower edge of the gap). Similarly, emission generally is dominated by $r_\perp \lesssim 0.3 r_{\rm LC}$, where $r_{\rm LC} = cP/2\pi$ is the light-cylinder radius. Accordingly, perturbations from particle inertia and currents will not be very strong in the low-density regions of the gap. We can therefore, with some confidence, take the magnetic field geometry to be the retarded potential vacuum dipole solution (e.g., Deutsch 1955), which lags increasingly from the static dipole solution as $\Omega \times r \to c$. While tedious to write analytically, the computation of these field lines is straightforward on the computer and forms the foundation of our gap geometry. Observations may eventually demand perturbations from the vacuum approximation which will provide details on the magnetosphere current structure.

We assume, following CHR, that there is a starvation gap starting near the intersection of the null charge (NC) surface and the surface of "last closed field lines" for which particles can corotate with the star. For comparison with future more complete treatments, we describe the gap in some generality. To specify this gap it is convenient to refer to the footpoints of various boundary field lines and their variation in magnetic polar angle with azimuth around the magnetic axis (Fig. 1). These include the lines tangent to the light cylinder which reach the star surface at $\theta_{\rm LC}(\phi)$ and the gap upper surface $\theta_g(\phi)$, where pair production begins to screen the rotation-induced $E_\parallel$. We also show the boundary of the closed zone at $\theta_{\rm cl}$, composed of lines parallel to $\Omega$ at $r_\perp \lesssim r_{\rm LC}$. The fractional width $w(\phi) = \theta_g/\theta_{\rm cl}$ of the gap also varies with azimuth around the polar cap. Note that the outer gap will span a fraction $\int w\, d\phi$ of the field lines in the open zone. It will be also convenient to refer to the fraction of the light-cylinder polar angle which is within the gap: $w'(\phi) = \theta_g/\theta_{\rm LC}$. Along the gap field lines we assume that the vacuum zone experiences a proportional fraction of the open field line potential drop, namely,

$$\Phi_{\rm gap} \sim \frac{1}{2}\left(\frac{\Omega r_*}{c}\right)^2 r_* B_s w\,, \qquad (1)$$

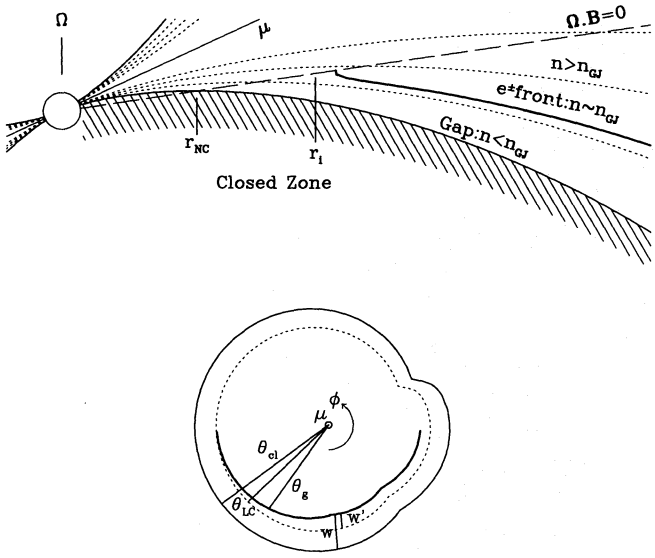





FIG. 1.—Outer magnetosphere gap geometry. *Above:* After initiation at radius $r_i$, continued pair production decreases the gap width with distance $s$ along the field lines. Here $\alpha = 65°$, and field lines are drawn in the $\Omega$-$B$ plane in the static dipole approximation. As drawn, the star radius is 40 times that for Vela parameters; note that inward-directed flux tangent to the gap surface will miss the star. *Below:* Footpoints of gap lines at the star surface. The dotted curve gives the lines tangent to $r_{LC}$ for $\alpha = 65°$ and the full retarded potential. The full open zone (*full line*) is slightly larger, while the asymptotic upper surface of the gap ($n \sim n_{GJ}$; *bold line*) defines a gap width varying with azimuth $\phi$.

where $B_s$ is the polar cap surface field and $r_*$ is the neutron star radius. The distribution of this potential drop along the gap from $\sim r_{NC}$ to the light cylinder depends on the details of the surrounding charge densities. CHR assumed a uniform drop, so that the acceleration field was $E_\parallel \approx \Phi_{gap}/r_{LC}$. If we assume that the field scales with $\boldsymbol{v} \times \boldsymbol{B}$, then we find $E_\parallel \sim r^{-2}$. Because particles are radiation-reaction limited, and because the range of radii is modest, we find that results do not depend strongly on the form of $E_\parallel$, but adopt $E_\parallel \sim r^{-1}$ in the following treatment.

We next assume that charges are created in this gap and that a modest fraction of the local corotation (Goldreich-Julian) charge density,

$$n_{GJ} = 7 \times 10^{10} B_z(r) P^{-1} \text{ cm}^{-3} , \quad (2)$$

experiences this acceleration field. These charges are limited by curvature radiation to

$$\gamma_{lim} = \left(\frac{eE_\parallel}{5.6 \times 10^{-3} mc}\right)^{1/4} \rho^{1/2}$$

$$\approx 5.1 \times 10^7 \left(\frac{X_e B_{12}}{P_{-1}}\right)^{1/4} \rho^{1/2} , \quad (3)$$

where the surface cap field is $B_s = 2 \times 10^{12} B_{12}$ G, $X_e \leq w$ is the fraction of the full open zone $E_\parallel$ field experienced by the particle, the pulsar period is $0.1 P_{-1}$ s, and the local field line radius of curvature $\rho$ is measured in units of $r_{LC}$. In general, $X_e < w$ when the screening charge density exceeds $n_{GJ}$ above the gap's upper surface. In this section we are interested in primary charges in the low-density gap itself, so that $X_e = w$. These charges emit a curvature spectrum with a cutoff energy

$$E_c \propto \gamma^3/\rho = 5.7 (X_e B_{12})^{3/4} P_{-1}^{-7/4} \text{ GeV} \quad (4)$$

for a typical radius of curvature $\rho \sim r_{LC}/2$ near $r_{NC}$. These photons comprise the main observed EGRET spectrum of the $\gamma$-ray pulsars, with spectral cutoffs from $\sim$1–10 GeV. Note that in traversing the outer gap, the primaries each radiate

$$n_\gamma \approx \frac{eE_\parallel r_{LC}}{2E_c} \approx 1.2 \times 10^5 \left(\frac{X_e B_{12}}{P_{-1}}\right)^{1/4} \quad (5)$$

peak photons.

As in the original CHR picture, we need pair production in the gap to tap the potential drop; with a magnetic field at $r_{NC}$ of $B_{NC} \sim 10^7 P_{-1}^{-3}$ G, only $\gamma$-$\gamma$ pair production is viable. The multi-GeV curvature photons pair produce most efficiently on a $\lesssim$1 keV background. This is provided by the thermal surface emission. Figure 2 shows a range of theoretical thermal luminosities (measured at infinity) for models with nonexotic interiors (after Ögelman 1995) and $r_* = 10^6$ cm. The corresponding surface temperatures remain above $\sim 10^6$ K for $10^5$ yr. For pulsars younger than $\sim 10^4$ yr or with very high fields, Ögelman notes that "magnetorotation" soft X-ray flux, powered by pulsar spin-down and to be identified with the gap emission, exceeds the thermal surface flux shown here. The drop-off in surface temperature after $10^6$ yr inhibits outer magnetosphere pair production. In our pulsar model primary photon aberration away from the field line direction ensures that pairs are initially produced with modest pitch angles $\psi \gtrsim 0.1$ and $\gamma \sim 10^{3.5}$; the perpendicular momentum is rapidly radiated away, giving a synchrotron spectrum peaking at $\sim$1–10 MeV (§ 4) that dominates the soft gap emission. The charges are also accelerated via $E_\parallel$ to join the radiation-reaction–limited primary population. As the particle population builds up beyond $n_{GJ}$, $E_\parallel$ decreases below its vacuum value; the resulting steep primary spectrum can give the curvature spectrum a softer index than the $E_\gamma^2 dN/dE_\gamma \sim E_\gamma^{+4/3}$ expected for monoenergetic curvature radiation.

The cross section for photon-photon pair production is

$$\sigma_{\gamma\gamma}(E_1, E_2) = \pi r_e^2 \{\beta_{cm}(\beta_{cm}^2 - 2) + (3 - \beta_{cm}^4) \ln [\gamma_{cm}(1 + \beta_{cm})]\}/\gamma_{cm}^2 , \quad (6)$$

where $\gamma_{cm} = \gamma^* E_1 (1 - \beta^* \cos \theta_1)/mc^2$. With the total angle between the incoming photons as $\theta = \theta_1 + \theta_2 = 2\theta_2 + \delta\theta$, where $\tan(\delta\theta/2) = \tan(\theta/2)(E_2 - E_1)/(E_1 + E_2)$, we can solve for the CM frame velocity as $\beta^* = (E_2 - E_1)/(E_2 \cos \theta_2 - E_1 \cos \theta_1)$, giving $\sigma_{\gamma\gamma}(E_1, E_2, \theta)$. The result is a cross section of $\approx 2 \times 10^{-25}$ cm$^2$ above a threshold $E_2$ of

$$\epsilon_{thr} \approx \frac{2(mc^2)^2}{(1 - \cos \theta) E_1} \quad (7)$$

for a primary $\gamma$ of energy $E_1$ incident at angle $\theta$. In practice, the optical depth for primary photons traveling through the magnetosphere is small, $\lesssim 10^{-3}$ to $10^{-2}$. Thus, while the bulk of the primary flux escapes to produce the observed beams, a small fraction of the $n_\gamma \sim 10^5$ primary photons produced by each primary charge produces pairs in the gap. The "gap closure" is self-regulating: if too many charges are produced, the vacuum width $w$ of the gap decreases, $E_\parallel$ and $E_c$ decrease, and $\epsilon_{thr}$ moves farther out on the Wien tail of the thermal surface distribution, decreasing the target photon cross section. Thus, as particles are produced along a given field line, the charge density builds up toward $n_{GJ}$;

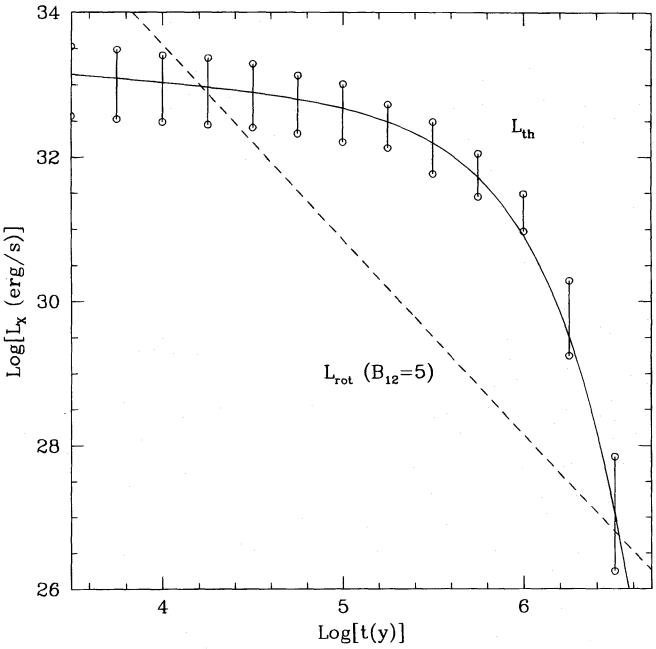


FIG. 2.—Soft X-ray luminosity evolution for young pulsars. The solid line approximates theoretical neutron star cooling curves for stars with nonexotic interiors (points delineate the range for detailed models). The dashed curve shows the empirical "magnetorotation" luminosity law proposed by Ögelman (1995) for $B_{12} = 5$.

beyond this point the line is above the gap, since the flow of charges along field lines ensures that $n \geq n_{GJ}$ at larger radii. As pair production continues for lines still in the gap, $n = n_{GJ}$ is obtained at decreasing gap thickness. However, as one moves away from the star, pairs are produced at decreasing efficiency, so that the fractional gap width stabilizes at an asymptotic value $w$ after a distance of order $r_{NC}$ (Fig. 1). Note that a constant $w$ gap grows in physical width as field lines diverge at large $r$. The gap width differs for each azimuth around the cap. Lines above $w$ will in general have $n \gtrsim n_{GJ}$, so there will be a density gradient above the gap.

Computing the gap width in detail is difficult, since the photon pair production depends critically on the angle $\theta$. There are two effects important to its computation. First, at high altitudes the primary photons will be aberrated ahead of their parent field line by the rotation and will thus have significant angle with respect to the largely radial surface flux; this increases the pair-production efficiency of photons originating in the outer magnetosphere. Field line curvature will abet this somewhat and will cause leading/trailing asymmetries in the gap width. Second, at low altitudes the stellar radius provides a finite angle for the photon cross section. In some cases it is also significant that soft thermal photons will be resonantly scattered in the charge-loaded regions of the closed zone. Thermal surface photons of energy $E_2$ will cross cyclotron resonance at

$$r_{res} = r_*(E_2/11.6B_{12}\ \text{keV})^{-1/3} \quad (8)$$

in the dipole field around the star. Daugherty & Harding (1989) give the resonance part of the photon scattering cross section as

$$\sigma(E) \approx \frac{\sigma_T}{2} \frac{E^2}{(E - E_{cyc})^2 + \Gamma_E^2}, \quad (9)$$

where $E_{cyc} = 11.6B_{12}$ keV and the natural line width due to excited-state decay is $\Gamma_E = 4/3\alpha m_c^2(B/4.4 \times 10^{13}\ \text{G})^2 = 2.6 \times 10^{-3} B_{12}^2(r)$ keV. This leads to a very narrow resonant region, and the scattering optical depth on the corotation density can be approximated as $\tau \sim (\sigma_T/2)(E_2^2/\Gamma_E^2)(r_{res}\Gamma_E/3E_2)n_{GJ}(r_{res}) \sim 2 \times 10^{-2}[B_{12}/(E_2/0.1\ \text{keV})]^{1/3}/P_{-1}$. Since the total $e^{\pm}$ density near the neutron star is likely to be many times the net charge density $n_{GJ}$ in the closed zone, it is likely that the resonant scattering of the soft thermal flux increases the apparent size of the neutron star for the outgoing photons. These regions are Thomson thin unless $n > 10^6 n_{GJ}$ for these periods, so there is an appreciable range of closed zone densities for which resonant scattering is the only substantial effect. This effect can be significant for low-$P$, high field pulsars, so it is included although it does not generally affect gap closure for pulsars older than Vela. The effect of resonant scattering on the pulse profile of the thermal surface flux will be described elsewhere (Romani & Rajagopal 1996).

Computation of the variation of the gap width with position in the magnetosphere involves following the population of curvature photons near $E_c$ as they propagate across field lines in the outer magnetosphere and tracing their conversion into pairs which subsequently travel along the field line at the pair production site. When the density from all pair production on a given field line reaches $\sim n_{GJ}$ the gap will be closed. The increasing particle density near the gap upper surface defines the locus of field lines on which tangentially beamed curvature and synchrotron radiation define the observed pulse as described in RY. Note that the described gap is *asymmetric*; since the bulk of the pairs in the high-$E_{\parallel}$ region are produced near the start of the gap, the outward-flowing charge will be reaccelerated and radiate $n_\gamma$ photons in traversing the gap. The opposite, inward-accelerated charge will rapidly cross the $\boldsymbol{\Omega} \cdot \boldsymbol{B} = 0$ surface and leave the strongly charge-depleted region. While we do then expect some inward-directed radiation, this flux will be much fainter than that of the outward beam and will be strongly beamed toward the spin equator. This should not contribute strongly to the observed pulsars viewed away from $\zeta = \pi/2$. Moreover, except for very highly inclined dipoles, most of this smaller flux will not impact the stellar surface, leading to greatly reduced surface heating (cf. Fig. 1). If the synchrotron flux from these regions exceeds the thermal surface flux, as observations of the $\tau \sim 10^3$ yr pulsars show (Ögelman 1995), then computation of gap closure will be a difficult self-consistency problem. However, when thermal surface flux dominates in the critical 100 eV–1 keV pair-production region, then simple approximate sums for the gap closure and pulsar efficiency can be obtained.

## 3. GAP CLOSURE AND EFFICIENCY EVOLUTION

An outer magnetosphere model should depend only on the spin parameters $P$ and $\dot{P}$ (represented here for comparison with data by characteristic age $\tau$ and dipole magnetic field $B$) and the magnetic inclination angle $\alpha$. Perturbations such as surface multipole structure, spin history, or external photon fluxes should have only weak effects in the gap zone. Although we can in principle compute the entire three-dimensional gap structure and pulsar beams, we start by computing characteristic gap sizes and beaming angles that will provide a pulsar $\gamma$-ray efficiency $\eta_\gamma(\tau, B, \alpha)$ according to the physical scheme in § 2.

The characteristic scale in the outer magnetosphere will

be

$$r_{LC} = 4.8 \times 10^8 P_{-1} \text{ cm} . \quad (10)$$

The intersection of the null charge zone with the last closed field line will vary with azimuth. Halpern & Ruderman (1993) estimate the radius of the null charge point in the $\Omega$-$B$ plane to be $r_{NC}/r_{LC} \approx (3 \tan \alpha/2)^{-2}$ for $\alpha \gtrsim \pi/4$. Since for $\alpha = 0$ $r_{NC}/r_{LC} = \frac{2}{3}$, in this paper we use $r_{NC} \approx [2(\pi/2 - \alpha)/3]^2 r_{LC}$. As the gap grows, the null charge intersection of the gap upper surface moves outward. Noting that we can relate the "closure radius" of the gap lines to the polar cap angle as in the static dipole solution and that the footpoint angle of the gap upper surface scales as $(1 - w)$, we write the radius of the gap closure point as

$$r_i \approx 2.1 \times 10^8 P_{-1} [(\pi/2 - \alpha)/(1 - w)]^2 \text{ cm} . \quad (11)$$

The finite size of the scattering surface in the closed zone ensures that the minimum photon-photon angle is $\sim r_{res}/2^{1/2} r_i$ where $r_{res}$ is given by equation (8). At higher altitudes the photon angles are dominated by aberration with $\theta \approx \pi r_i/2 r_{LC} \approx 0.7[(\pi/2 - \alpha)/(1 - w)]^2$.

Taking the typical field line radius of curvature in the gap to be $\bar{\rho} \sim r_{LC}/2$, we can adopt equations (4) and (5) for $E_c$ and $n_\gamma$ and compute the pair production on the thermal surface flux. The evolution of the neutron star surface temperature is adequately described by $T(t) = 10^6$ K$(t/10^5$ yr$)^{-0.05}$ exp $(-t/10^6$ yr) (giving the solid line in Fig. 2) out to several times $10^6$ yr. Complications due to nonthermal surface spectra induced by neutron star atmospheres (e.g., Rajagopal & Romani 1996; Shibanov et al. 1992) are ignored here, as are heated polar caps or the additional soft X-ray flux produced by the gaps themselves. Comparing the pair-production threshold energy (eq. [7]) with the thermal peak, and taking $1 - \cos\theta \approx \theta^2/2$, we see that

$$\frac{\epsilon_{thr}}{kT} \approx 2.1 \frac{P_{-1}^{7/4}}{\theta^2 T_6 (X_E B_{12})^{3/4}} . \quad (12)$$

Thus for typical pulsar conditions we will be on the Wien tail of the thermal surface spectrum and the soft photon density above threshold will be

$$n_2 \approx \frac{2\sigma T^3}{kc} \left(\frac{\epsilon_{thr}}{kT}\right)^2 e^{-\epsilon_{thr}/kT} \left(\frac{r_*}{r_i}\right)^2 . \quad (13)$$

Finally, to compute the gap width we compute the pair multiplication factor $n_{mul} = n_\gamma n_2 \sigma_{\gamma\gamma} r_i$; taking $X_E = w$, we can then solve $n_{mul}(w) \approx 1$ for the width at which particle multiplication is in equilibrium, with each primary producing $\sim 1$ secondary pair, and gap closure occurs.

In this model, the total potential drop (and hence the energy deposited in curvature photons per primary) scales as the fractional gap width $w$. Moreover, the total number of charges participating will be proportional to the gap width, so we expect the efficiency to be quadratic in $w$. Since the field lines initially curved away from the spin axis are the ones closed at moderate altitude, we adopt

$$\eta_\gamma = w\left(w - \frac{w^2}{2}\right) n_{mul}(w) , \quad (14)$$

which accounts for the gap's rough behavior as a half-annulus and where the final factor of $n_{mul}$ accounts for the low charge density in only partially closed gaps. The model is clearly not complete for very large $w$ or very small $\alpha$, so we restrict $r_i$ to be $\leq r_{LC}$ and $w \leq 0.75$ in numerical computations.

In addition to $\eta_\gamma$, the fraction of the spin-down power converted to MeV–GeV photons, it is important to estimate $f_\gamma$, the beaming factor of these $\gamma$-rays on the sky. As shown in YR, this determines both the solid angle over which a given pulsar will be observable (centered on the spin equator) and the apparent $\gamma$-ray luminosity for observers within the beam. For example, if the true beaming factor is $f_\gamma$ but a beaming factor of 1 is assumed (i.e. isotropic radiation), the *inferred* pulsar efficiency will be $\eta = \eta_\gamma/f_\gamma$. Although a detailed model for the $\gamma$-ray beam at each $\tau$, $B$, and $\alpha$ is needed for a precise value for $f_\gamma$ we can adopt here the following fit to the models plotted in YR (Fig. 1):

$$f_\gamma = \left(\frac{\alpha}{80^\circ}\right)^{1/2} \frac{(1 - w')}{(1 + w')} , \quad (15)$$

which is accurate to better than $\sim 20\%$ over most of the parameter range.

Together these estimates give $\eta_\gamma(\tau, B, \alpha)$. Figure 3 shows the efficiency variation with characteristic age for $\alpha = 65^\circ$ and several values of $B$. In addition to the true efficiencies, we show the efficiencies inferred for a beaming factor of 1 sr, along with the $E > 100$ MeV efficiencies for several EGRET pulsars (Fierro 1996), again with an *assumed* $f_\gamma = 1/4\pi$.

Several features are worth noting. First, efficiencies increase strongly with spin-down age and are also higher for large-$B$ objects at a given $\tau$, such as PSR 1758−23 if identified with the coincident EGRET source (low field objects such as PSR 1951+32 are conversely less efficient). This is because for large $B$ and $\tau$ the pulsar spin period $P = 0.248 B_{12} \tau_6^{1/2}$ s increases, so that the light-cylinder radius and $r_{NC}$ increase. This makes gap closure more difficult; with a larger $w$, a higher efficiency and smaller $f_\gamma$ result.

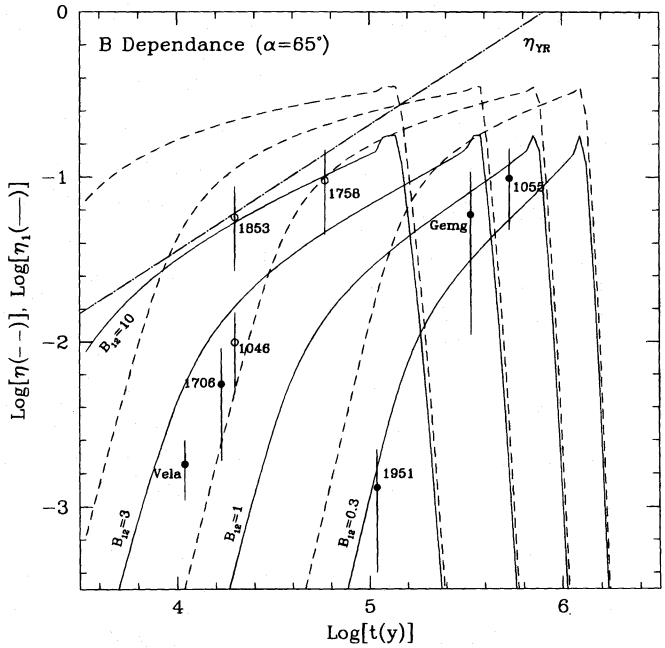


FIG. 3.—Efficiency ($\eta_\gamma$) evolution for the high-energy flux of young pulsars with various values of $B$ and with $\alpha = 65^\circ$ (*dashed lines*). Also shown are the *inferred* luminosity variations $\eta_1$ (*solid lines*) for an assumed fixed $f_\gamma = 1/4\pi$. Data points give the corresponding inferred 100 MeV–2 GeV efficiency ranges from EGRET observations of $\gamma$-ray pulsars (*closed circles*) and candidate unidentified sources (*open circles*) from Fierro (1996); again $f_\gamma = 1/4\pi$ is assumed. For comparison the dotted line gives the single-parameter efficiency estimate of YR. Throughout, $P = 0$ at birth and constant $B$ are assumed.

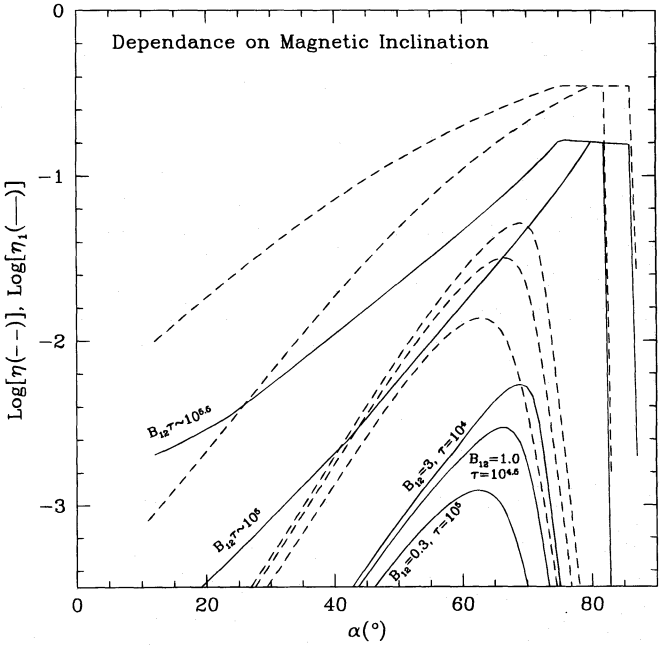


FIG. 4.—True (*dashed lines*) and 1 steradian beam ($f_\gamma = 1/4\pi$) estimates (*solid lines*) for $\gamma$-ray pulsar efficiency variation with magnetic inclination angle $\alpha$. Curves show the variation for several combinations of $B$ and $\tau$.

The steep fall-off in $\eta_\gamma$ for $\tau < 10^4$ yr is partly due to the relatively large soft photon angles imposed by the circumstellar resonant scattering. If the closed zone does not contain sufficient density to allow this scattering, $\eta_\gamma$ will be somewhat larger in this region. Note, however, that for high $B$ this is also the region where magnetospheric flux can dominate surface emission; this unincluded flux will conversely decrease somewhat the predicted efficiencies for young pulsars. Note that only pulsars with relatively low fields $B_{12} \lesssim 1$ will persist as bright $\gamma$-ray sources at ages $\sim 10^6$ yr. The steep fall-off at large ages is due both to the growth of $r_i$ and to the rapid fall-off in the surface $T$ beyond $10^6$ yr. By comparing the true efficiency curves with the curves for $f_\gamma = 1/4\pi$, one sees that the true beaming factors are large for inefficient pulsars, but drop to $\sim 10\%$ for highly efficient pulsars. Thus, although the true $\gamma$-ray efficiencies are only 0.2–0.3 for these objects, if isotropic emission is assumed one will infer $\gamma$-ray luminosities exceeding the total spin-down power.

In Figure 4 we display the dependence on magnetic inclination $\alpha$. For old pulsars large inclinations provide for small $r_{NC}$. This in turn limits the contribution of aberration to $\theta$ and promotes high $\gamma$-ray efficiency. In computing $n_{mul}$ it is found that in this regime the gap self-limits, so that the exponent in equation (13) is nearly constant. This implies that $P^{7/4} \propto B^{3/4}$. Since $P \propto B\tau^{1/2}$, this in turn ensures that $\tau^{7/8} \propto B^{-1}$. Therefore, pulsars with $\tau B \sim$ constant have similar efficiency variation. For younger pulsars the algebraic factors become significant and the behavior is more complex; $\eta_\gamma$ peaks near $\alpha \sim 65°$. Note that, as in Figure 3, the $\eta_{obs}$ values inferred for inefficient pulsars are much smaller than the true values if $f = 1/4\pi$ is assumed.

## 4. RADIATION SPECTRUM

The curvature radiation power spectrum from a primary with energy $\gamma_e mc^2$ is

$$P(E) = E^2 \frac{dN}{dt\,dE} = \frac{3^{1/2} e^2 \gamma_e E}{h\rho} F_{syn}\left(\frac{E}{E_c}\right) = 6.02 \times 10^7 \frac{\gamma_e E_{MeV}}{\rho} F_{syn}\left(\frac{E}{E_c}\right) \text{ MeV s}^{-1}, \quad (16)$$

where $E_c$ is the cutoff energy (eq. [4]) and $F_{syn}(x) = x \int_y^\infty K_{5/3}(y)dy$. For $E \ll E_c$ this gives the sharply rising spectrum $P(E) \propto E^{4/3}$. While recent observations of $\gamma$-ray radiation from efficient old pulsars and phase-resolved analysis of other objects indicates photon number spectra as hard as $dN/dE \sim E^{-1.3}$, it has long been known that younger objects such as Crab and Vela exhibit a softer spectrum. Of course, a steep soft spectrum of primary electron energies can produce a softer curvature spectrum over a modest range.

As charges are produced and accelerated above $r_i$, we expect two effects that can generate a spectrum of radiation-reaction–limited particles. First, near $r_i$ particles on a given field line will experience a range of $E_\parallel$ as they pass to regions of decreased $w$ and higher charge density (Fig. 1). Second, $E_\parallel$ should not drop abruptly to zero but should exhibit some penetration of the increasingly dense plasma at the gap upper surface. For concreteness, we posit that $X_e \propto n_{GJ}/n$ for $n > n_{GJ}$ and that charge increase has approximately constant scale length transverse to $B$. A careful treatment of the charge and field distributions around the gap will be needed to see whether the anomalous resistivities required for this field penetration ansatz are present or whether we will need to rely on the acceleration history at the gap onset to supply the electron energy spectrum. Note that our ansatz gives $dN_e/dE_\parallel \propto E_\parallel^{-1}$, and thus, as long as the particles are radiation-reaction limited (eq. [3]), this gives rise to a steep soft electron energy spectrum $dN_e/dE_e \propto E_e^{-p}$ with $p = 4$. The electron spectrum will reach radiation reaction energies as long as $t_{acc} = \gamma mc^2/eE_\parallel c$ is less than $t_{fl} = P/2\pi$. For the acceleration potential (eq. [1]) this leads to the condition

$$X_E > 3.8 \times 10^{-3} \frac{P_{-1}^2 \gamma_7}{B_{12}} \quad (17)$$

to reach Lorentz factors of $10^7\gamma_7$. This electron spectrum causes the curvature spectrum to develop a broad maximum with power spectrum $E^2 dN/dE \sim E^{-(p-5)/3} \sim E^{1/3}$ (i.e. photon number spectrum $dN/dE \sim E^{-1.7}$) This spectrum will extend from $E_c \sim 3$ GeV down to $E_b \sim E_c X_{E,min}^{3/4} \sim 20$ MeV for parameters similar to Vela's. Below this break energy the curvature spectrum will harden toward $P(E) \sim E^{4/3}$ from single-particle curvature radiation. For longer period or lower field pulsars such as Geminga and PSR 1055−52, $X_{E,min}$ will be much larger and the GeV spectrum will approach $E^{-1}$ as the particle spectrum becomes more nearly monoenergetic. In general, we expect the spectral index to be correlated with $\eta_\gamma$.

Since photons are aberrated across field lines, pairs are initially produced with significant pitch angles, $\psi \sim 0.1$, and initial Lorentz factors, $\gamma_i \sim E_c/2 \sim 3 \times 10^3 (X_E B_{12})^{3/4} P_{-1}^{-7/4}$. Near the null charge line these will emit synchrotron radiation, delivering a spectrum with an upper cutoff

$$E_{syn} = 0.5 X_E^{3/2} B_{12}^{5/2} P_{-1}^{-13/2} (r_i/0.1 r_{LC})^{-2} \text{ MeV}, \quad (18)$$

taking as a rough approximation $\psi \sim r_i/r_{LC}$. For Vela parameters this gives $E_{syn} \sim 2$ MeV, while for the Crab

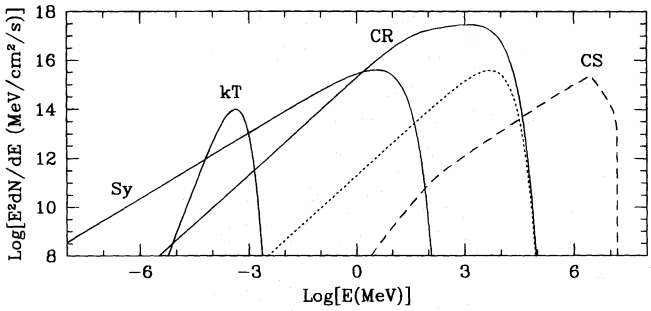


FIG. 5.—Characteristic phase-averaged spectrum for a young $\gamma$-ray pulsar ($B_{12} = 3$, $E_c = 3$ GeV). Solid lines show the curvature spectrum (CR), the synchrotron emission near $r_i$ (Sy) and the thermal surface flux (kT) described in § 4. For comparison, the dotted curve gives the monoenergetic primary curvature spectrum with the same $E_c$ as for CR. The dashed curve gives the TeV pulsed spectrum from Compton upscattering of the synchrotron spectrum on the primary $e^{\pm}$.

$E_{\rm syn} \gtrsim 300$ MeV. Since $E_\parallel$ acceleration does not counter pitch-angle losses, the electrons cool, resulting in $dN/dE_\perp \sim E_\perp^{-p}$ with $p \approx 1$. The corresponding synchrotron spectrum is $P_{\rm syn}(E) \sim E^{-(p-3)/2} \sim E^{+1}$. This flatter spectrum will dominate the curvature emission for $E < E_{\rm syn}$. Note that since $P_{\rm syn}(E) \propto B(E/E_{\rm syn})^{1/3} \sim B^{1/6}$, there will be a weak increase in $P_{\rm syn}$ at a given $E$ for high field pulsars. We can also estimate the ratio between the total curvature power, $P_{cr} \sim E_C n_\gamma \sim \Phi_{\rm gap}$, and the total synchrotron power, $P_{\rm syn} \sim \gamma_i n_{\rm mul} \sim E_C n_2(r_i)\sigma_{\gamma\gamma} r_i$, by noting that $P_{\rm syn}/P_{cr} \sim \tau_{\gamma\gamma} \sim 3 \times 10^{-3}$ for gaps controlled by thermal surface flux. For short-period, high-field pulsars such as the Crab and PSR 1509−58, synchrotron flux will dominate the thermal surface emission. In this case, we expect that $n_2(r_i)$ will substantially exceed that due to the thermal surface flux and $\tau_{\gamma\gamma}$ will increase toward unity, giving a power-law nonthermal spectrum at keV–MeV energies, and spectra peaking below the EGRET range. Figure 5 shows the schematic phase-averaged pulsar spectrum, including thermal surface flux, curvature radiation, and synchrotron emission for $\tau \sim 10^{4.5}$ yr and $B_{12} = 3$.

## 5. PHASE-RESOLVED EGRET SPECTRA: VELA MODEL

The pulsar spectrum of the previous section shows many features present in the phase-averaged spectra collected by Thompson (1996). It is, however, important to remember that these estimates are based on characteristic values for $r_i$, $\theta$, etc. Since these quantities vary with position in the magnetosphere, we expect spectral variations through the pulsar profile. Such variations can be noted by comparing pulse profiles from different energy ranges; for example, in our model we expect power-law synchrotron emission from near $r_i$ to be present in the X-ray light curves of young pulsars, leading to power-law tails in *ROSAT* spectra, peaked between the $\gamma$-ray maxima for viewing angles $\zeta$ not too far from $\pi/2$. We also can follow variations in the curvature spectrum near the peak. For the brighter EGRET pulsars, high-quality phase-resolved spectra are now available, so we can compare the predictions of our outer magnetosphere radiation model with these data.

To implement the gap closure model of § 2 in a local manner, we must follow the photon beams as they propagate to the light cylinder, crossing field lines and converting on the thermal photon flux. The buildup of charges with distance $s$ along a given field line then determines the locus of the gap radiation surface and the local value for $w(\phi, s)$. Such models produce asymmetric gaps with variation along the surface of last closed lines (work in preparation). As an intermediate step we can, however, trace photons and charges along a single line to confirm the basic behavior described in §§ 2 and 3. As an example, we will estimate gap closure and radiation for the Vela pulsar, which has the best count statistics in the EGRET data.

The gap closure sums of § 3 predict $w = 0.17$ for Vela-like parameters [$\log(\tau) = 4.04$, $B_{12} = 3.3$, $\alpha \approx 70°$]. Adopting the potential drop $\Phi_{\rm gap}$, distributed as $r^{-1}$, we have computed an approximate value for $w$ along several lines spaced around the polar cap by taking the curvature photon flux to be that produced at lower altitudes on the same line. These photons are allowed to pair produce on the thermal surface spectrum of a generic 10 km, $10^6$ K neutron star, using the detailed kinematics of equation (6). While Ögelman (1995) finds a slightly larger $T_{\rm eff}$ and smaller effective area, results are insensitive to these modest spectral changes. For field lines curved toward the equator, we find that the gap reaches a stable width at $w = 0.17$–$0.24$; this asymptotic value is reached within a path length $\delta s < 0.03 r_{\rm LC}$ along the asymptotic field line. This supports the values for the gap closure estimates in § 3. Since cross-field propagation is not presently included, we cannot examine the variation of the gap width with $\phi$. We can, however, estimate the phase-averaged spectrum and illustrate variations in pulse phase by following the changes in charge populations with position for a characteristic gap shape.

For a specific choice of $\theta_{\rm cl}$, we define the last closed field lines as those parallel to $\Omega$ at $r_{\rm LC}/2^{1/2}$ (where the corotation velocity equals the Alfvén speed; cf. Henrickson & Rayburn 1974), this provides a polar cap $\sim 2^{1/4}$ times larger than the simple vacuum value (Fig. 1). Then, adopting a constant $w = 0.2$ gap width, $\alpha = 65°$, and a rotation-axis–line-of-sight angle $\zeta = 79°$ as in RY, we find the location of the emission region on the upper surface of the gap viewed as a function of pulsar phase. The altitude of the emission point at each phase, along with the distance from the null charge surface $\delta s$, is shown in Figure 6. Superposed for phase reference is a light curve generated assuming uniform outward-beamed emissivity along the gap surface. The observed GeV light curve is adequately modeled by this pulse, although additional pulse structure can arise in this outer magnetosphere picture from weak inward-directed flux, charges on high-altitude field lines, and, at lower energies, wide beaming of the gap emission (see RY). The radio pulse occurs at phase 0. Note that in the interpulse region emission occurs lower in the magnetosphere and closer to the null charge surface.

Our trace of $w(r)$ along a typical field line allows us to estimate $E_\parallel(r)$ in the gap but does not accurately reproduce the buildup of charge beyond $n \sim n_{\rm GJ}$. We therefore allow the maximum charge density to increase in proportion to $\exp(\delta s/0.1 r_{\rm LC})^2$ as pair production continues over a distance $\sim r_i$. Charges are injected with $\gamma = 10^{7.5}$ and allowed to come into radiation-reaction equilibrium as they flow along the gap. This prescription allows the particle population to extend to lower energies as $X_{E,\rm min} \propto 1/N$ decreases higher in the gap. The result is a narrow distribution of electron energies near $r_i$, spreading over a factor $\sim 3$ in $E_e$ as $\delta s$ approaches $0.3 r_{\rm LC}$. We next compute the full curvature spectrum as a function of pulse phase for the Earth line of sight at $\zeta = 79°$ and compare with observed EGRET spectra.

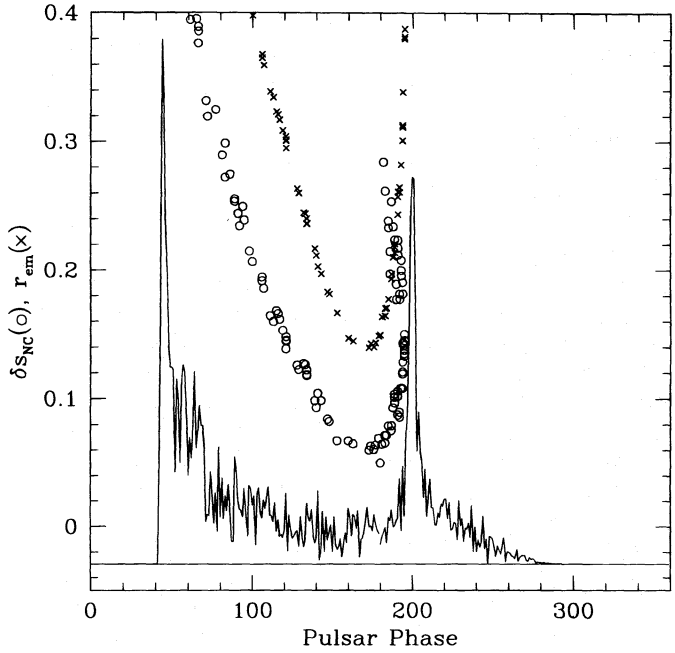


FIG. 6.—Variation of the emission point as a function of pulse phase for Vela. Crosses give the radius of the (lower) emission point in units of $r_{LC}$; open circles give the distance from the null charge surface in the same units. For reference, the solid line gives a pulse profile for uniform emissivity along the gap. The radio pulse and closest approach of the magnetic axis are at phase 0.

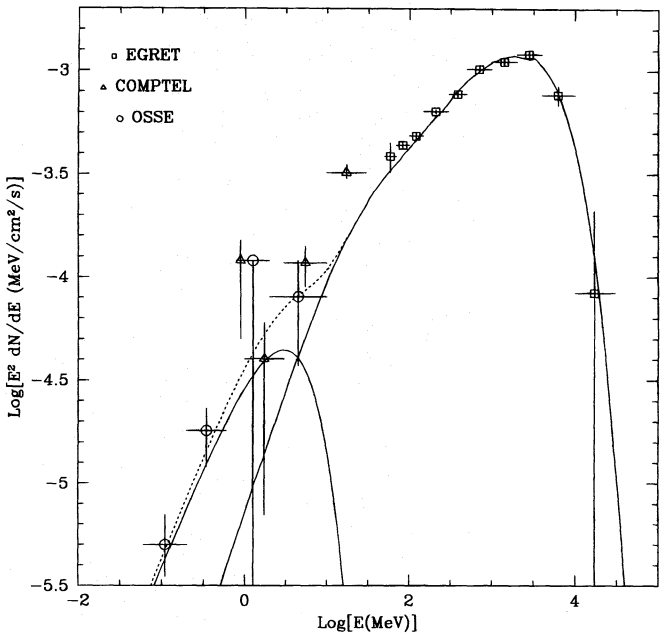


FIG. 8.—Phase-averaged spectra for Vela compared with *CGRO* data. The solid lines give the curvature and synchrotron spectra (dashed line is sum) for the Vela model observed at the Earth line of sight. EGRET data points are from the pulsed spectra of Fierro (1996); OSSE and COMPTEL points are from Strickman (1996) (after Daugherty & Harding 1996).

In Figure 7, EGRET phase-resolved spectra from a pulsed analysis (Fierro 1996) are shown for the first peak, the second peak, and the interpulse region. Pulsed analysis avoids contamination from a soft spectral component, largely unpulsed, which is likely background flux and also allows spectra to be extended above 10 GeV. The model spectra, computed for the same phase range as the corresponding data, reproduce the details of the phase variations quite well, although the components have been individually normalized. In the constant-$w$ model described, the first pulse is slightly too bright and the second pulse is too weak by a factor of 3. It is likely that this will be rectified in a three-dimensional computation with variable gap width, since the leading emission of P1 from large $r$ is aberrated more strongly, leading to a narrower gap, while the increased width in the P2 region will result in a larger local curvature efficiency. It is encouraging that this test computation produces spectral slope variations in the 100 MeV to GeV range very close to those seen and phase-varying high-energy rollovers consistent with the data. Note that this model predicts significant 10–30 GeV flux in contrast to polar cap pair cascade models.

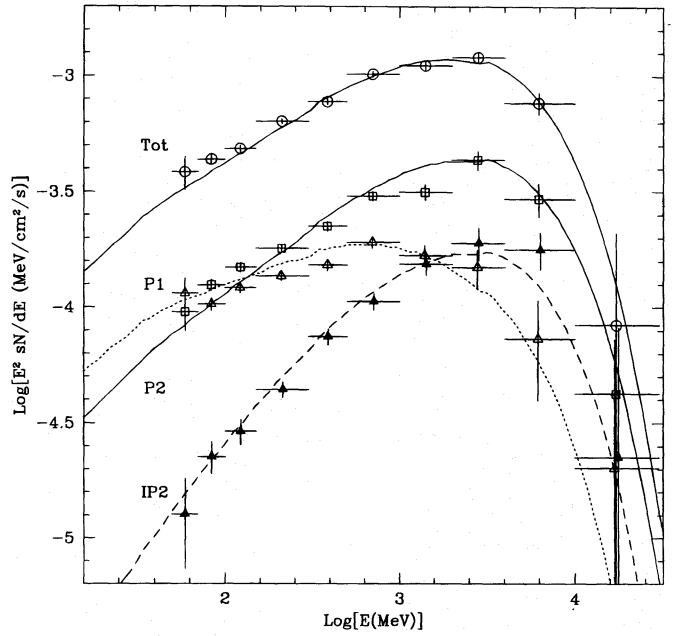


FIG. 7.—Phase-resolved spectra for the Vela pulsar. Data points are from a pulsed analysis for the first peak (P1), an interpulse zone (IP2), the second pulse peak (P2), and the total flux (Fierro 1996). Model curves for the same phase intervals and Vela parameters have assumed a constant gap width $w = 0.2$ and followed the evolution of the electron and photon spectra along the resulting gap.

The phase-averaged sum of the pulse components is shown in Figure 7 and over a broader energy range in Figure 8, combining data from three *CGRO* instruments. Here we also plot the estimated synchrotron spectrum with $E_{syn}$ following equation (19) and the synchrotron/curvature flux normalization $F_{syn}/F_{cr} = 10^{-3.5}$. Changes in the viewing angle can significantly affect this soft component, which here rises above the $E < E_B$ portion of the curvature spectrum.

## 6. DISCUSSION AND CONCLUSIONS

We have outlined the physics of gap closure and curvature and synchrotron radiation in the outer magnetosphere. This model predicts efficiencies and beaming fractions for GeV pulsars in good accord with the data. Significant dependence of $\eta_\gamma$ on the pulsar magnetic field was found. Since the $\gamma$-ray emission is also quite sensitive to the magnetic inclination $\alpha$ (which, along with the spin parameters $B$ and $\tau$, completely determines the pulsar properties), careful polarization observations and models of the radio profile to constrain $\alpha$ for young pulsars are particularly important.

A test computation with a constant gap width $w$ in this picture produces an encouraging match to the spectra and phase variations of the Vela pulsar. This success depends, however, on a steep ($dN/dE \sim E^{-4}$) electron spectrum extending for a factor $\sim 3$ in energy; we have provided a physical ansatz that motivates such a spectrum, but detailed gap electrodynamics are needed to substantiate this picture. These results should also be substantiated by computations following the variation of $w$ for various gap field lines and for other pulsars (work in preparation), but it seems likely that the modeled spectral variations will be quite robust. The tendency of older, more efficient pulsars toward harder spectra is natural in this model; photon number spectral indices approaching $-1$ can be expected for some phases of old pulsars, but there should always be significant curvature in the 100 MeV to GeV range, so that power laws will not provide adequate fits to high-quality data.

The computations in this paper have been directed to pulsars with ages greater than or similar to that of Vela for which thermal surface emission should dominate the flux in the sub-keV range. Pulsars such as Crab, PSR 0540−69, and PSR 1509−58 are clearly dominated by nonthermal power laws at these energies. We infer that this flux is synchrotron radiation from the outer magnetosphere and that larger $\tau_{\gamma\gamma}$ will ensure copious pair production and small $w$ and GeV curvature $\gamma$-ray efficiencies. In the case of the Crab (and possibly PSR 0540−69) the synchrotron photons will contribute significantly to the EGRET flux; for PSR 1509−58, $E_{\rm syn} \sim 2$ MeV, so the spectrum will peak in the COMPTEL range. Computations of gap closure will be more difficult for synchrotron-dominated pulsars, since, as in the original CHR model, both the high-energy photons and the soft target flux are produced by the gaps themselves. Closure itself will, however, remain much easier than in the CHR scheme because of the modest pair-creation optical depth required.

Since these $\tau \sim 10^3$ yr pulsars will have pair creation extending well above $r_{\rm NC}$, it is tempting to interpret likely emission differences in the light of observations of the Crab pulsar. First, with $\tau_{\gamma\gamma} \lesssim 1$ we can expect the magnetospheric pair-creation rate to be $n_\gamma w A_{\rm cap} n_{\rm GJ} c \sim 10^{38} e^{\pm}$ s$^{-1}$ for Crab parameters. This is consistent with the pair content inferred from observations of the plerion, although further particle acceleration is required in the wind shock. The continued production of pairs out to $r \sim r_{\rm LC}$ gives rise to the sharp optical pulses from the outer gap region. The Crab gaps are thus also much more symmetric than those of Vela and other older objects; weak absorbed emission from inward-directed beams crossing the magnetosphere may be expected. It also seems likely that the dense pair plasmas in the high-altitude gaps are what give rise to the coherent radio emission from these regions exhibiting giant pulses and spectral peculiarities. Finally, there is the question of the field lines that curve away from the pulsar spin equator, cross the spin axis, and reach the $\boldsymbol{\Omega} \cdot \boldsymbol{B}$ surface near $r_{\rm LC}$ opposite the standard outer gap zones (these connect with the normal gap at large radii but may be thought of as equivalent to the "short" gaps of CHR; see Fig. 1 of this paper). Normally these gaps do not close well and contribute only weakly to the $\gamma$-ray emission. However, if we assume that the strong pair creation at large $r_i$ in the Crab allows these to be active and trace the expected pulsed flux for the Earth line of sight, we find two pulse components lagging P2 by $\sim 60°$ and $\sim 100°$. It is intriguing that recent 4.8 GHz radio observations show two additional pulse components at these phases (Moffet & Hankins 1996). It will be interesting to see whether these components exhibit giant pulses and related radio phenomena and to see whether careful analysis of apparent off-pulse structure in the EGRET Crab data can detect weak $\gamma$-ray emission at these phases.

Finally, we can estimate the inverse Compton scattering (ICS) of the primary electrons on soft photons from the pulsar gap. The $\gamma \sim 10^{7.5}$ primaries will most efficiently upscatter $10^{-2}$ eV (IR) photons from the low-energy end of the synchrotron spectrum. Most of this scattering is in the Klein-Nishina regime, where Blumenthal & Gould (1970) give the upscattered number spectrum as

$$\frac{dN}{dt\,dE} = \frac{2\pi r_0^2 c}{\gamma_e^2} \frac{n_{\rm syn}(E_2) dE_2}{E_2} \times \left[ 2q \ln q + (1+2q)(1-q) + \frac{(\Gamma_e q)^2 (1-q)}{2(1+\Gamma_e q)} \right], \quad (19)$$

with $\Gamma_e = 4E_2 \gamma_e / mc^2$, $q = E_1/\Gamma_e(1-E_1)$, and $E_1 = E/\gamma_e mc^2$. Without a careful computation of the synchrotron beaming, it is difficult to estimate the photon density $n_{\rm syn}(E_2)$ at these energies in the gap. Roughly, though, we can expect $E_\gamma\, dN_\gamma/dE_\gamma \sim$ constant for our synchrotron spectrum. Comparing with the flat power law synchrotron flux at thermal peak, we typically have $n_2 \sim 10 n_{\rm syn}$ for $10^4$ yr, $B_{12} = 3$ pulsars while $\sigma_{\rm T} \approx 3\sigma_{\gamma\gamma}$, so we expect $\tau_{\rm ICS} \sim 3 \times 10^{-3}$, scaling from the estimates of § 4. Integrating the upscattering over the primary population $N(\gamma_e)$ down to the cutoff from the minimum $X_E$ (eq. [17]), we obtain the TeV Compton spectrum shown in Figure 5. This *pulsed* TeV flux containing somewhat less than 1% of the pulsed GeV flux is an attractive target for future air Cerenkov experiments.

Support for this work was provided by NASA grants NAGW-2963 and NAGW-4526. Helpful discussion on pulsar physics with J. Arons, R. Blandford, J. Fierro, and I.-A. Yadigaroglu, as well as important clarifying questions raised by the referee, are also acknowledged. The Institute for Theoretical Physics at UCSB is thanked for hospitality during the preparation of this report.

## REFERENCES

Arons, J. 1981, in Plasma Astrophysics, ed. T. D. Guyenne & G. Levy (ESA SP-161; Paris: ESA), 273
Arons, J., & Scharleman, E. T. 1979, ApJ, 231, 851
Blumenthal, G. R., & Gould, R. J. 1970, Rev. Mod. Phys., 42, 237
Chen, K.-Y., & Ruderman, M. A. 1993, ApJ, 408, 179
Cheng, K. S., Ho, C., & Ruderman, M. A. 1986, ApJ, 300, 522 (CHR)
Chiang, J., & Romani, R. W. 1992, ApJ, 400, 629
———. 1994, ApJ, 436, 754
Daugherty, J., & Harding, A. K. 1989, ApJ, 336, 861
———. 1996, ApJ, 458, 278
Dermer, C. D., & Sturner, S. J. 1994, ApJ, 420, L75
Deutsch, A. J. 1955, Ann. d'Ap., 18, 1
Fierro, J. 1996, Ph.D. thesis, Stanford Univ.
Halpern, J. P., & Holt, S. S. 1992, Nature, 357, 222
Halpern, J. P., & Ruderman, M. 1993, ApJ, 415, 286
Harding, A. K., & Daugherty, J. 1993, in Isolated Pulsars, ed. K. A. van Riper, R. Epstein, & C. Ho (New York: Cambridge Univ. Press), 279
Helfand, D. J. 1994, MNRAS, 267, 490
Henrickson, R. N., & Rayburn, D. R. 1974, MNRAS, 166, 409
Holloway, N. J. 1973, Nature, 246, 6
Kanbach, G., et al. 1994, A&A, 289, 855
Moffett, D., & Hankins, T. 1996, ApJ, submitted
Morini, M. 1983, MNRAS, 202, 495
Ochelkov, Yu. P., & Usov, V. V. 1980, Ap&SS, 69, 439

Ögelman, H. 1995, in Lives of Neutron Stars, ed. A. Alpar, U. Kizilglu, & J. van Paradijs (Dordrecht: Kluwer), 101
Rajagopal, M., & Romani, R. W. 1996, ApJ, 461, 327
Romani, R. W., & Rajagopal, M. 1996, in preparation
Romani, R. W., & Yadigaroglu, I.-A. 1995, ApJ, 438, 314 (RY)
Shibanov, Yu. A., Zavlin, V. E., Pavlov, G. G., & Ventura, J. 1992, A&A, 266, 313
Strickman, M. 1996, ApJ, submitted
Sturner, S. J., Dermer, C. D., & Michel, F. C. 1995, ApJ, 445, 736
Thompson, D. J. 1996, preprint
Thompson, D. J., et al. 1996, ApJS, 101, 259
Usov, V. V. 1994, ApJ, 427, 394
Yadigaroglu, I.-A., & Romani, R. W. 1995, ApJ, 449, 211 (YR)
———. 1996, ApJ, submitted